A 70-dB SNR High-Speed Global Shutter CMOS Image Sensor for *in Situ* Fluid Concentration Distribution Measurements

Tetsu Oikawa[ID], Rihito Kuroda[ID], *Member, IEEE*, Keigo Takahashi, Yoshinobu Shiba, Yasuyuki Fujihara[ID], Hiroya Shike[ID], Maasa Murata[ID], Chia-Chi Kuo[ID], Yhang Ricardo Sipauba Carvalho da Silva, Tetsuya Goto[ID], Tomoyuki Suwa, Tatsuo Morimoto, Yasuyuki Shirai, Takafumi Inada, Yushi Sakai, Masaaki Nagase, Nobukazu Ikeda, and Shigetoshi Sugawa, *Member, IEEE*

Abstract—**This article presents a global shutter (GS) high signal-to-noise ratio (SNR) and a high-frame-rate CMOS image sensor (CIS) for *in situ* fluid concentration distribution measurements using absorption imaging. The pixel consists of a ultraviolet (UV)-visible-near infrared (NIR) waveband pinned photodiode (PD) with high robustness against UV light irradiation for various measurement objects, two-stage lateral overflow integration capacitors (LOFIC) for high dynamic range and high SNR, and a voltage-domain memory bank for GS. The developed prototype CIS with 22.4-μm pitch pixels exhibited 69.7-dB maximum SNR, 123-dB dynamic range, and 1000-frames/s maximum frame rate under single exposure GS and successfully captured images of dynamic movement of NO_2 gas concentration distribution in the vacuum chamber for 300-mm-diameter wafers.**

Index Terms—**Absorption imaging, CMOS image sensor (CIS), global shutter (GS), lateral overflow integration capacitor (LOFIC), signal-to-noise ratio (SNR), wide dynamic range (WDR).**

I. INTRODUCTION

PRACTICAL realization of smart ways of manufacturing, agriculture, and healthcare is critical to improve the productivity and sustainability of our society. In these

fields, next-generation Internet-of-Things (IoT) technologies with high-precision image sensors having high signal-to-noise ratio (SNR) for analytical applications [1], [2] are needed. In particular, *in situ* measurement technologies that can measure and visualize the concentration distribution of dynamically moving gases and liquids by noninvasive/nondestructive manners are expected to be useful in various fields. For example, real-time visualization of gas concentration distribution inside process chamber of semiconductor manufacturing equipment would greatly improve process control as well as process diagnosis.

Several concentration measurement methods using light absorption have been utilized in high-performance liquid chromatography with linear array sensor [3], [4], gas concentration sensor with a single photodiode (PD) [5], and so on. Equation (1) shows the SNR of image sensors

$$\text{SNR} = 20 \log_{10} \left(\frac{N_{\text{sig}}}{\sqrt{\sqrt{N_{\text{sig}}^2} + n_{\text{sys}}^2}} \right) \cong 20 \log_{10} \sqrt{N_{\text{sig}}} \quad (1)$$

where N_{sig} is the number of signal electrons and n_{sys} is the number of input-referred system noise electrons. Equation (1) shows that if the system noise is sufficiently small under high illumination and the photon shot noise dominates the total noise, then the SNR can be increased. This can be done by using a powerful light source and a sensor with a high full-well capacity (FWC) to capture small light absorption. In conventional methods with linear array sensors or single point detectors, high FWC has been achieved by using a large PD or attaching a large capacitor to the PD. To acquire concentration distribution information with high accuracy by absorption imaging, an image sensor with extremely high FWC pixels needs to be developed. For instance, to achieve 70-dB SNR, over 10-Me$^-$ FWC is needed.

There are several technologies to increase FWC, such as using organic photoconductive with high-density capacitors [6], [7], complementary carrier collection [8], and lateral overflow integration capacitor (LOFIC) [9]–[11]. In the LOFIC method, PD, FD, and LOFIC can be optimized independently. Besides its linear response, it is considered that LOFIC is suitable for high-precision absorption imaging.
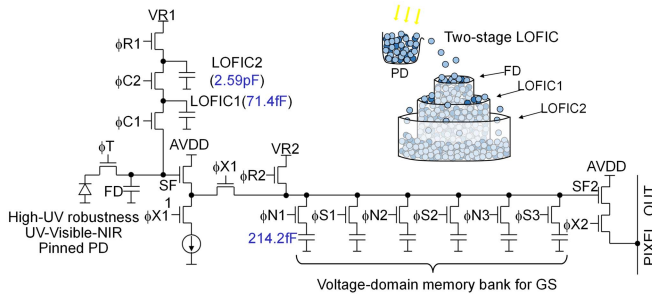
Fig. 1. Pixel circuit diagram of the developed CIS.

Fig. 2. Pixel layout diagram.

Fig. 3. Pixel cross-sectional diagram.

In addition to high SNR, there are other requirements for absorption imaging. First, high-speed and global shutter (GS) operation is desirable to capture fast-moving objects without distortion, such as gases in the semiconductor process chamber. When measuring the concentration of individual substances in mixture gases or liquids, it is necessary to switch the light sources or optical filter with the appropriate wavelengths. Here, the GS is advantageous to efficiently synchronize the exposure period and the light illumination period. Due to the high-density capacitor technologies reported in recent years [12]–[15], the noise performance of the voltage-domain GS CMOS image sensor (CIS) has been improved. In addition to the GS function, a wide spectral response covering ultraviolet (UV), visible to near infrared (NIR) is also required to capture the light absorption of various materials.

In the IISS International Image Sensor Workshop (IISW) 2021, a 27.8-Me⁻ FWC GS CIS with two-stage LOFIC and voltage-domain in-pixel analog memory bank both formed by Si trench capacitor was reported to be useful for this purpose [16]. In this article, we additionally discuss in detail the design and the characteristics of the developed CIS for absorption imaging. Also, gas concentration imaging experiments with high-resolution optical systems using telecentric lens were also conducted. Section II shows the structure and the operation of developed CIS, Section III shows the measurement results and discussion, and the conclusion is given in Section IV.

II. Developed CIS

A. Circuit Architecture and Operation

Figs. 1 and 2 show the pixel circuit and layout diagrams of the developed CIS. The pixel consists of an front side illuminated (FSI) pinned PD, a transfer gate (T), a first source follower driver (SF1), a current source, a current source switch (X1), a first overflow switch (C1), an LOFIC1, a second overflow switch (C2), an LOFIC2, a reset gate (R1), a memory bank reset gate (R2), a voltage-domain memory bank, a second source follower driver (SF2), and a select switch (X2). The memory bank contains six sample/hold circuits for storing light and reference signals for the highest sensitivity signal (S1 and N1), high saturation signal (S2 and N2'), and the highest saturation signal (S3 and N3'). PD has a highly concentrated surface P⁺ layer with steep dopant profile for high sensitivity and robustness toward UV light. In addition, 20-μm-thick epitaxial
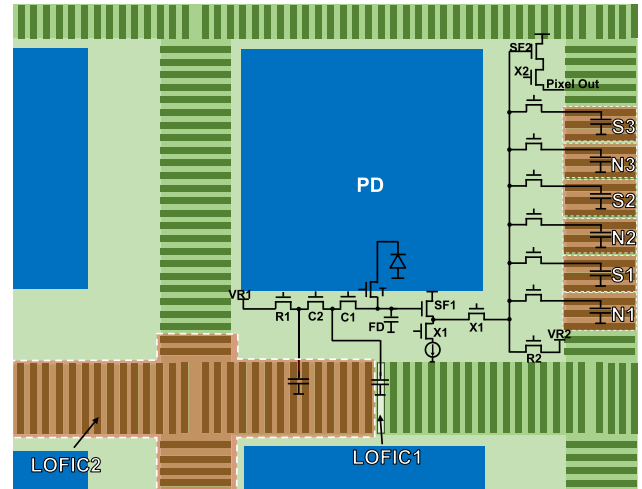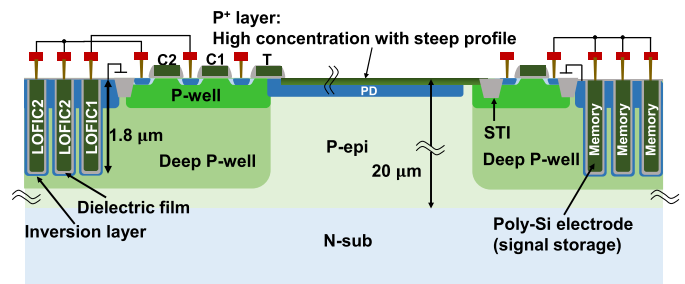
P-type Si layer enhances the sensitivity to NIR light. PD with this structure have been reported to have sensitivity across a wide range of wavelength from 200 to 1100 nm, and the degradation of sensitivity and the increase in dark current due to UV light were suppressed for practical applications [17], [18]. High-density Si trench capacitors [12] were employed for LOFIC1 (71.4 fF), LOFIC2 (2.59 pF), and the memory bank (214.2 fF each) that consist of 1, 37, and 3 units of capacitor cells, respectively. Here, the unit capacitor cells with the same layout were employed for both LOFIC and analog memory bank for high process uniformity. The capacitance values of LOFIC1 and LOFIC2 were designed to achieve 70-dB maximum SNR and sufficiently high SNR at signal switching points, especially at the S2 and S3 signal for absorption imaging as to be explained later. Also, the capacitance of the memory bank was designed to sufficiently reduce the thermal noise.

Fig. 3 shows the pixel cross-sectional diagram of developed CIS. The Si trench capacitors consist of a buried poly-Si electrode for signal storage, SiO₂ dielectric film, and inversion layer as the counter electrode on the Si substrate side. The trench depth is 1.8 μm. The potential of inversion layer is fixed to ground (GND) or a constant voltage. The highly reliable SiO₂ dielectric was employed to achieve low leakage current and low trap density. In this configuration and structure, signal storage node does not suffer from p-n junction leakage current or surface recombination current. Also, as the signal storage node is electrically shielded by the fixed voltage electrode,
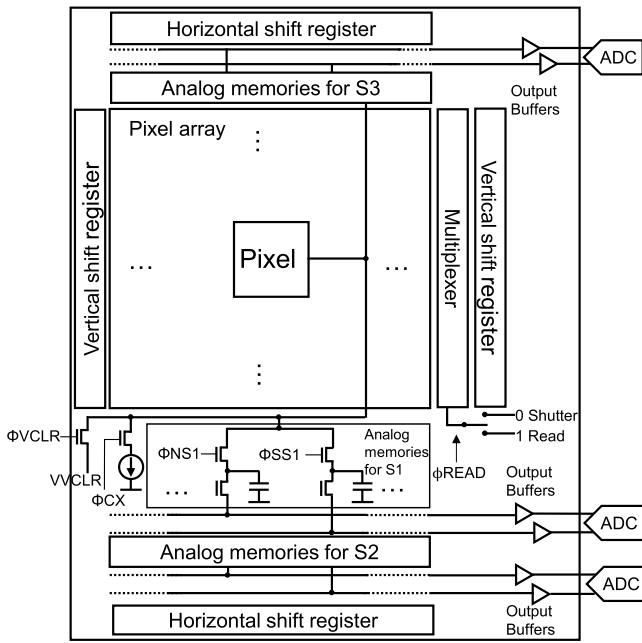
Fig. 4. Circuit block diagram.

Fig. 5. Pixel potential diagram under high illumination condition.

Fig. 6. Pixel timing diagram.

Fig. 7. Row-by-row readout operation timing diagram.

and the capacitance values are large, the effect of coupling between stored signals and control pulses is small. In addition, the trench capacitors are surrounded by a deep p-well (DPW) to prevent leakage between the PD and the inversion layer of trench capacitors. The concentration of DPW was optimized to suppress the leakage and to obtain a high uniformity of the capacitance value over the operating voltage range. Detailed information of optimizations of trench capacitor formation process and DPW conditions as well as transmission electron microscope (TEM) images of the trench capacitors can be seen elsewhere [11], [12]. In addition, distances between adjacent edges of PDs are arranged equally in all the directions to reduce the variation of crosstalk by making the potential between pixels symmetrical. This is especially important for measurements using NIR light with a long penetration length.

Recently, a GS CIS for soft X-ray detector with two-stage LOFIC and voltage-domain memory bank was reported to be useful for wide dynamic range (WDR) soft X-ray imaging [19]. In this work, the gate sizes of the drive transistors for SF1 and SF2 as well as the current sources were designed to enable 1000-frames/s operation. The driving current for SF1 is 6 μA in this work.

Fig. 4 shows the circuit block diagram of developed chip. It consists of pixel array, analog memory for pixel output, vertical and horizontal shift registers (VSR and HSR) for signal readout, and output buffers. The three differential pairs of high sensitivity, high saturation, and the highest saturation signals are readout in parallel and the A/D conversion is performed by off-chip ADCs. The multiplexer selects the operation modes: the GS operation mode and the row-by-row readout operation mode by controlling ΦREAD. The HSR operates at 40 MHz for 1000-frames/s operation.

Fig. 5 shows the potential diagram and Figs. 6 and 7 show the GS and readout operation timing diagrams, respectively. In the GS operation, ΦREAD is set to low. Under a high illumination condition, photoelectrons overflown from the PD are accumulated in LOFIC1 and LOFIC2 (t1). The reference signal for the high sensitivity signal is readout by SF1 and stored in N1 memory (t2). Photoelectrons in the PD are transferred to FD (t3). A high sensitivity S1 signal is readout at FD (t4), a high saturation S2 signal is readout at FD + LOFIC1 (t5), and the highest saturation S3 signal is read out
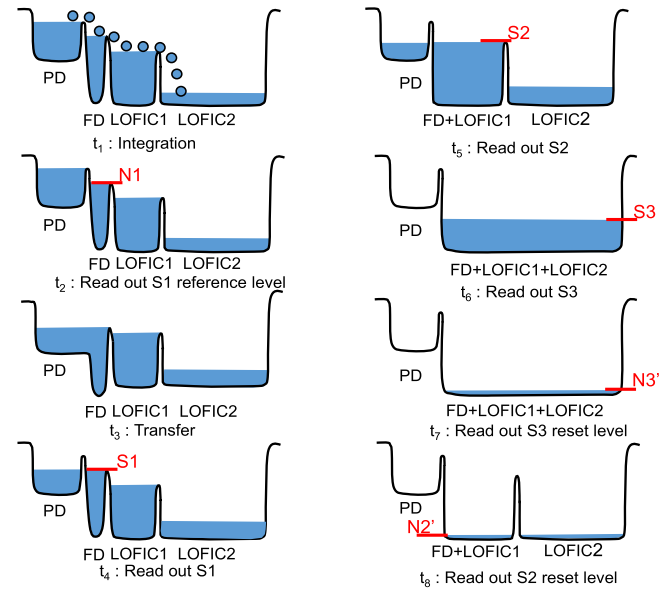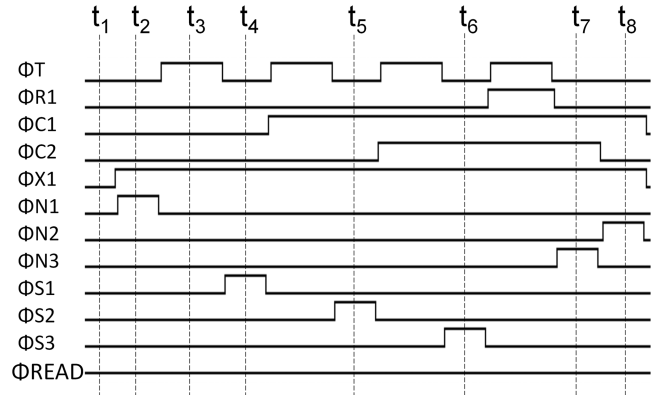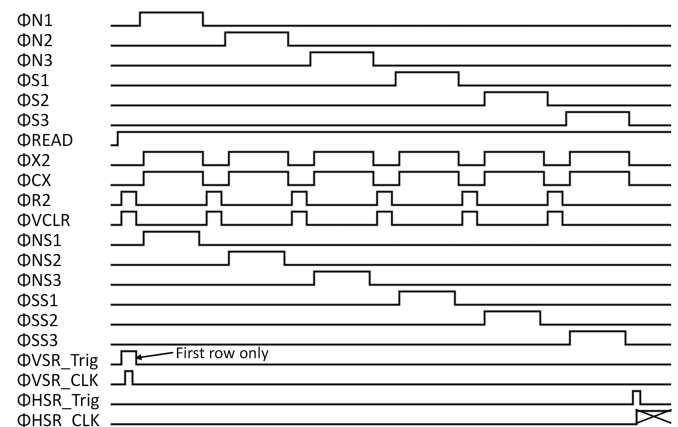
Fig. 8.   Micrograph of the developed chip.

Fig. 9.   Photoelectric conversion characteristics.

at FD + LOFIC1 + LOFIC2 (t6); they are stored in the S1, S2, and S3 memories, respectively. Then, PDs are reset by R1, the reset signal for the highest saturation signal is read out at FD + LOFIC1 + LOFIC2 (t7), and the reset signal for th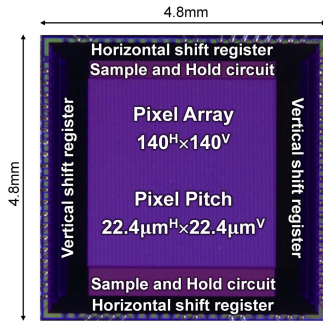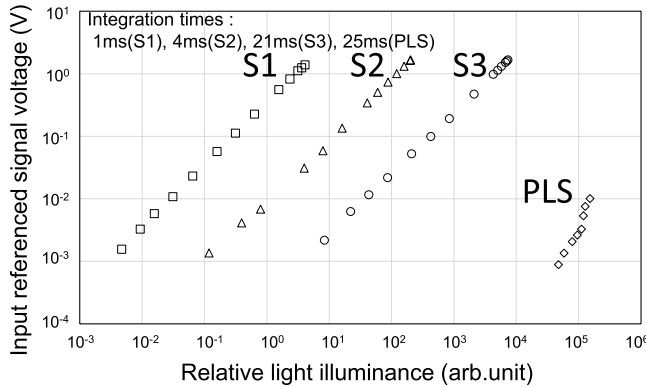e high saturation signal is read out at FD + LOFIC1 (t8); they are stored in the N3' and N2' memories. After all signals are readout, ΦREAD switches to high, and the readout operation and the integration time for the next frame start. With this operation, the time aperture ratio is higher than 99% at 1000 frames/s, which enables stagger-free shutter operation. The signal of the row selected by the VSR is output to the column analog memories via the vertical signal line and readout by the HSR to the horizontal signal line sequentially and outputted by the output buffers for digitization using the onboard ADC. A column-parallel ADC architecture can be introduced to the developed CIS.

B. Chip Fabrication

Fig. 8 shows the micrograph of the developed chip. The developed CIS was fabricated using a 0.18-μm one-poly-Si five-metal CIS process technology with pinned PD. The power supply voltage is 3.3 V, and the die size is 4.8 mm^H × 4.8 mm^V. The pixel size and the number of the effective pixels are 22.4 μm^H × 22.4 μm^V and 140^H × 140^V, respectively.

III. Measuremet Results and Discussion

Fig. 9 shows the measured photoelectric conversion characteristics. A green LED was used as the light source, and the integration times for S1, S2, and S3 signals were 1, 4, and
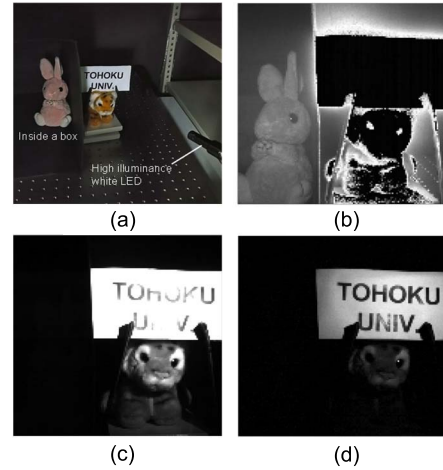

Fig. 10.   (a) Image shooting samples and sample images captured by (b) high sensitivity S1 signal, (c) high saturation S2 signal, and (d) highest saturation S3 signal.

21 ms, respectively. Here, all signals with different sensitivities were measured with different integration times to measure them with the same light source. A WDR performance of 123-dB was obtained under a single exposure by GS. The dark random noise of S1 during this measurement was 18 e$^-_{rms}$. To form the overflow path of the LOFIC without pixel-to-pixel variation, measurements were made by adjusting the counter electrode voltage of the trench capacitor and the voltage when the overflow switch is turned off. For the fabricated chips in this work, when these voltages were set to prioritize the overflow efficiency, it resulted in an increase of dark current and its shot noise. We consider that this dark current component is coming from the inversion layer of the trench capacitors to the PD, and it can be reduced by optimizing the layout, process condition for the DPW, and the voltage setting. As for the signal readout noise, the total temporal noise is 6.5 e$^-_{rms}$ and the kTC noise of the analog memory is about 2.3 e$^-_{rms}$. The parasitic light sensitivity (PLS) characteristics are also shown in the same figure. The sensitivity ratios between S1, S2, and S3 and the parasitic light signal at the in-pixel memory were −145, −113, and −81.7 dB, respectively. There are three main reasons why small PLS was achieved. First, diffusion layers of the switch transistor of the analog memory were sufficiently shielded by the shield metal. Second, in analog memory, the buried electrodes of trench capacitor are used to store signal voltage, which is free from the inflow of photogenerated charges. Third, due to the large capacitance ratio between FD and analog memory, the signal electrons are greatly amplified by SF1. Due to these methodologies, small PLS has been achieved.

Table I shows the photoresponse nonuniformity (PRNU) characteristics and circuit gain nonuniformity including SF1. They were 0.93% and 0.62% for S1, 0.61% and 0.45% for S2, and 0.61% and 0.41% for S3. For the measurement of the circuit gain nonuniformity, the voltage level of the input node of SF1 was first set to variable VR1 through the reset gate R1, and then, the input node of the SF1 was set floating when measuring the output. The circuit gain nonuniformity is the dominant source of the PRNU for S2 and S3 signals. Thus,
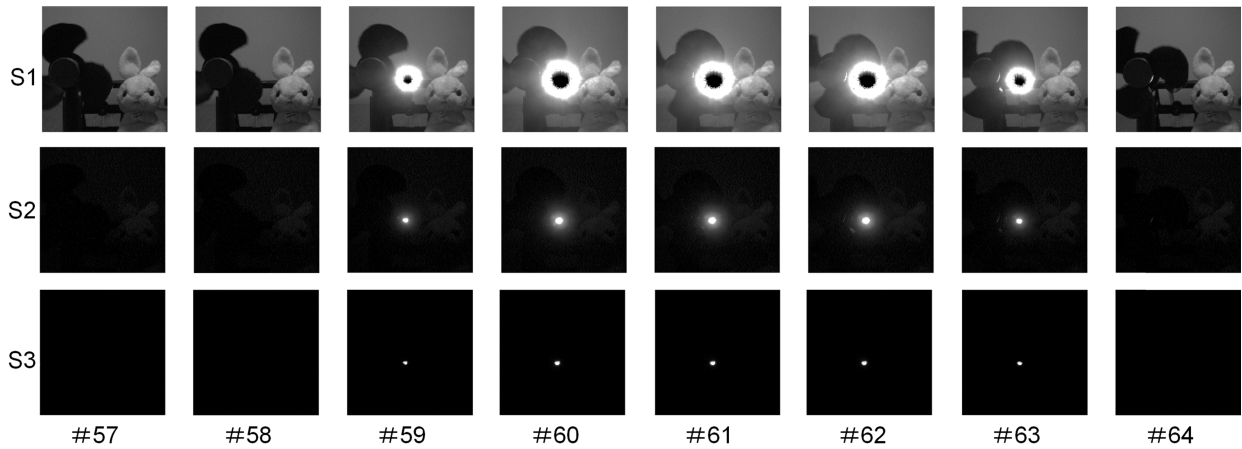
Fig. 11. Sample images demonstrating high-speed GS and low PLS performances.

TABLE I
PRNU CHARACTERISTICS

Signal	PRNU (%)	Circuit gain non-uniformity (%)
S1	0.93	0.62
S2	0.61	0.45
S3	0.61	0.41

Fig. 12. SNR characteristics.

Fig. 13. Gas concentration distribution measurement system using absorption imaging for semiconductor manufacturing equipment.

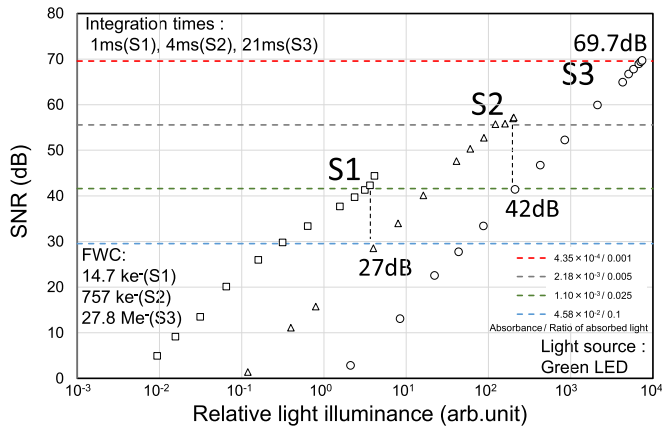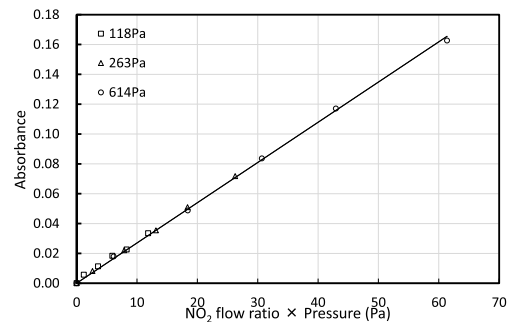Fig. 14. Acquired calibration curve extracted from the obtained images. The product of gas flow ratio and pressure corresponds to the gas concentration in vacuum chamber.

the effect of trench capacitor introduction to the LOFIC is small in terms of PRNU.

Fig. 10 shows the sample images captured by developed CIS. Three regions with different illuminances were prepared using a high illuminance white LED and a box for light shielding, and the images were taken using a lens with a frame #4 with a 4-ms integration time. Fig. 10(a) shows the image shooting samples captured by another camera with the light source turned off. The images of Fig. 10(b)–(d) were captured by S1, S2, and S3, respectively. Developed CIS demonstrated the wide dynamic range (WDR) performance by single exposure GS.

Fig. 11 shows the sample images to validate GS and low PLS performances. A high-intensity white LED was illuminated from the behind the fan rotating at about 2000 r/min and they were captured at 1000 frames/s. The integration time

and the maximum signal storage time at in-pixel memory were 0.5 and 1 ms, respectively. The LED light intensity was set at about 90% of the saturation level of S3, which is more than 1500 times higher than the saturation level of S1. GS operation was clearly confirmed without image distortion of the moving fan. Also notably, at frame #58, it is one frame prior to the light source to appear in the captured image. It is the most severe condition in terms of PLS as the light source illuminated the image sensor surface during the signal readout period of frame #58. Including frame #58, there was no effect of PLS confirmed in the captured images of S1, S2, and S3.
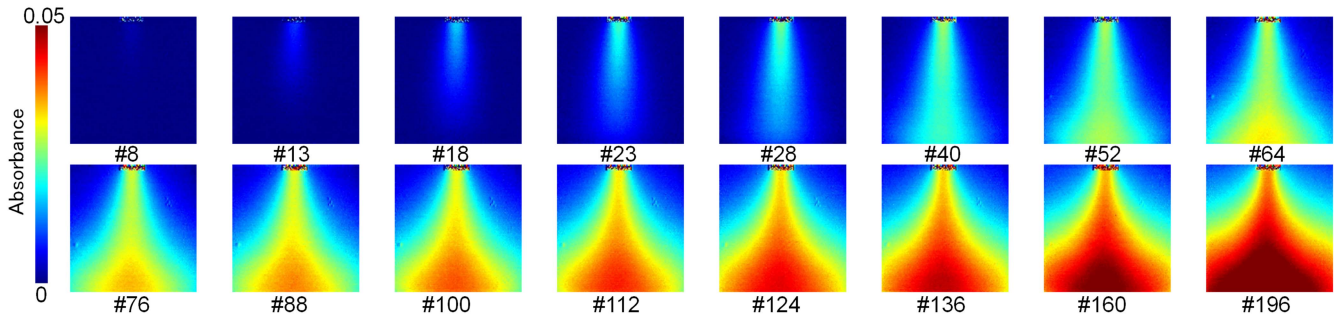
Fig. 15. Captured images of dynamic movement of NO$_2$ gas flow in the vacuum chamber at 1000 frames/s. Supplied gas switched Ar to NO$_2$ at 667 Pa (# corresponds to the frame number).

Fig. 12 shows the measured SNR characteristics. The maximum SNR of 69.7 dB was obtained by the S3 signal. The FWCs of S1, S2, and S3 were 14.7 ke$^-$, 757 ke$^-$, and 27.8 Me$^-$, respectively. Here, the obtained SNR characteristics are discussed as follows regarding the required SNR to distinguish the slight change of light due to absorption. For the accurate absorption imaging, the difference of the signal electron (Δn) due to the light absorption should be larger than the noise by a factor α as in the following equation:

$$\Delta n = n_{I_0} - n_{I_1} > \alpha \cdot n_{\text{tot}} \qquad (2)$$

where n_{I0} and n_{I1} are the numbers of signal electrons with and without light absorption, respectively, and n_{tot} is the input-referred total noise in electron. The following equation shows the definition of the absorbance:

$$A = -\log \frac{I_1}{I_0} \qquad (3)$$

where I_0 and I_1 are the intensities of incident light and transmitted light, respectively. For the linear response image sensors, I_1/I_0 is assumed to be equal to n_{I_1}/n_{I_0}. From (2) and (3), Δn is expressed by the following equation:

$$\Delta n = n_{I_0}\left(1 - 10^{-A}\right). \qquad (4)$$

Consequently, the minimum SNR required to detect an absorbance A is obtained as follows:

$$\text{SNR} = 20\log \frac{n_{I_0}}{n_{\text{tot}}} > 20\log \frac{\alpha \cdot n_{I_0}}{\Delta n} = 20\log \frac{\alpha}{1 - 10^{-A}}. \qquad (5)$$

In this study, the required SNRs were calculated with $\alpha = 3$. In Fig. 12, the horizontal dotted lines show the SNR values required to detect absorbance or ratio of absorbed light $1 - I_1/I_0$ to the incident light for several cases. According to Fig. 12, the minimum detectable absorbance for the developed image sensor is about 4.35×10^{-4}. In addition, for the developed image sensor dedicated to absorption imaging, the SNR at the switching point between S2 and S3 was designed to be higher compared to that of the switching point between S1 and S2. By this design, the light illumination range available for absorption imaging can be higher. For instance, the absorbance of 1.10×10^{-3} or higher can be detected for over 2.5 decades of light illumination range including at the switching point from S2 to S3.

As discussed above, the high SNR is critically important for high-precision absorption imaging to detect subparts per million order of fluid concentration. By always turning on the transfer gate and LOFIC switches to hold only the S3 signal and by using the six S/H capacitors in the memory bank to perform correlated multiple sampling, the FWC can be further increased and the thermal noise and low-frequency noise of the first source follower can be reduced, respectively, to further improve the SNR.

The SNR characteristics of the developed CIS shown in Fig. 12 does not include fixed pattern noise (FPN). SNR was calculated using only temporal noise at room temperature due to the following circumstances. In absorption imaging, absorbance A is calculated from the ratio of I_0 and I_1 as in (3). In a pixel, the light intensities in voltage signal are obtained as in the following equations using the number of incident photons without light absorption η_0 and with light absorption η_1, the quantum efficiency (QE), and the conversion gain CG

$$I_0 = \eta_0 \cdot \text{QE} \cdot \text{CG} \qquad (6)$$
$$I_1 = \eta_1 \cdot \text{QE} \cdot \text{CG}. \qquad (7)$$

In these equations, I_0 and I_1 are calculated as voltage signal amplitudes with respect to the same dark level of each pixel, so the dark signal nonuniformity (DSNU) is canceled in this image processing. In addition, QE and CG vary among pixels, which causes PRNU. The variations of QE and CG are also canceled when calculating absorbance for each pixel as long as these characteristics are constant for the signal range. Thus, the high linearity of signal is very important. Consequently, the LOFIC technology, which can achieve large FWC with high linearity is highly advantageous in absorption imaging applications.

Fig. 13 shows the developed gas concentration distribution measurement system. In semiconductor manufacturing process such as atomic layer deposition (ALD), chemical vapor deposition (CVD), and etching, the control of the process gas concentration in the vacuum chamber is important for the atomic scale uniformity across the entire wafer substrate. The measurement system consists of the developed CIS, the vacuum chamber with six 150 mm^H $\times$ 50 mm^V windows designed for the gas concentration visualization, a gas supply system, and a 405-nm LED as light source. The wavelength

TABLE II
PERFORMANCE SUMMARY AND COMPARISON WITH OTHER GS CISs

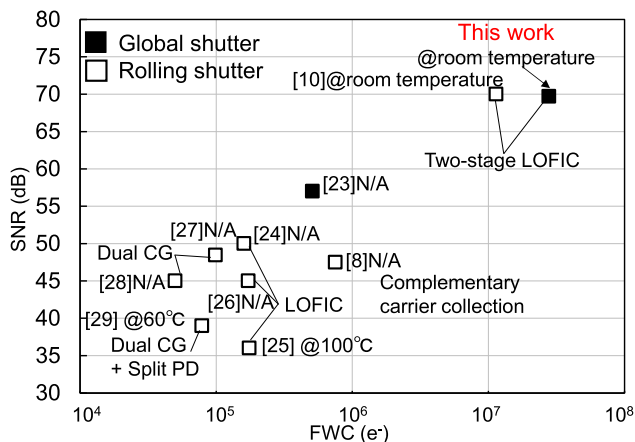|	This work	C. Liu [20]	K. Miyauchi [21]	Y. Kumagai [22]
GS type	Voltage domain	In-pixel ADC	Voltage domain	Charge domain
Process technology	0.18 μm FSI	45 nm CIS/65 nm stacked BSI	45 nm/65 nm stacked BSI	65 nm /90 nm stacked BSI
Power supply voltage	3.3 V	N/A	N/A	3.3 V/1.8 V/1.2 V
Die size	4.8 mm^H×4.8 mm^V	4 mm^H×4 mm^V	8 mm^H×8 mm^V	N/A
# of effective pixels	140^H×140^V	512^H×512^V	1024^H×832^V	3208^H×2184^V
Pixel size	22.4 μm^H×22.4 μm^V	4.6 μm^H × 4.6 μm^V	4 μm^H × 4 μm^V	2.74 μm^H × 2.74 μm^V
Fill factor	41%	100%	100%	100%
Maximum Frame rate	1,000 fps	480 fps	N/A	190 fps@12bit 260 fps@10bit
Conversion gain	94.4 μV/e⁻(S1) 2.19 μV/e-(S2) 60.1 nV/e-(S3)	170 μV/e⁻(PD) 7 μV/e⁻(FD)	N/A	N/A
FWC	14.7 ke⁻(S1) 757 ke⁻(S2) 27.8 Me⁻(S3)	3.8 ke⁻(PD) 51 ke⁻(FD) 9 Me⁻(TTS)	7 ke⁻(HCG) 130 ke⁻(LCG)	10 ke⁻
PLS	-145 dB(Mem/S1) -113 dB(Mem/S2) -81.7 dB(Mem/S3)	-55 dB(FD/PD) <-140 dB(Mem/PD)	<-140 dB	-80 dB
Maximum SNR	69.7 dB	N/A	< 50 dB	N/A
Dynamic range	123 dB	127 dB	90 dB	74 dB

Fig. 16. Maximum SNR and FWC as benchmarking of developed CIS with other RS and GS CIS with high saturation performance. The measurement temperatures are shown in the graph.

corresponds to an absorption peak of NO$_2$ gas, which is used as the measurement target. Here, NO$_2$ is often used for nitridation process for electron devices. By using three sets of sensors and light sources to capture images from three directions, this measurement system can measure the 3-D concentration distribution. As a preliminary experiment, the 2-D concentration distribution of NO$_2$ gas in the vacuum chamber was visualized.

Fig. 14 shows a calibration curve of absorbance obtained from the captured images for various gas flow ratio and pressure conditions. The obtained results show good linearity among various process conditions.

Fig. 15 shows the absorbance images of NO$_2$ gas in the vacuum chamber captured by the S3 signal using frame #25 telecentric lens. Here, telecentric lens allows only rays of light parallel to the optical axis to transmit. It is useful to improve

spatial resolution as well as for the 3-D image construction of gas concentration distribution. The transient state of switching from Ar to NO$_2$ gas at a total flow rate of 50 sccm supplied from a nozzle with an outer diameter of 1/4 in at a pressure of 667 Pa and 23 °C was visualized for a 32 mm^H × 32 mm^V cross section of the chamber at 1000 frames/s. Diffusion of gas supplied real-time measurement system is useful to improve process condition as well as for the abnormal state detection of semiconductor equipment.

Table II shows the performance summary of the developed chip and comparison with other GS CISs.

Fig. 16 shows the relationship of maximum SNR and FWC, compared with other high saturation CIS for UV-visible-NIR imaging reported in recent years with provided chip measurement temperatures [8], [10], [23]–[29]. The developed CIS achieved 27.8-Me⁻ FWC and 69.7-dB maximum SNR under single exposure GS operation.

IV. CONCLUSION

A 22.4-μm pixel pitch GS CIS with two-stage LOFIC and voltage-domain memory bank was developed, and its performance was demonstrated. The developed chip achieved 69.7-dB maximum SNR, 123-dB DR, and 1000-frames/s maximum frame rate. Due to its high SNR and high frame rate, the developed CIS successfully acquired images from the moving NO$_2$ gas in vacuum chamber with a linear calibration curve. The developed CIS is the key to the *in situ* fluid concentration distribution measurements for various applications.

REFERENCES

[1] T. Pakpuwadon *et al.*, "Self-reset image sensor with a signal-to-noise ratio over 70 dB and its application to brain surface imaging," *Frontiers Neurosci.*, vol. 15, p. 714, Jun. 2021.

[2] C. Cao *et al.*, "Signal-to-noise ratio enhancement in cardiac pulse measurements using multitap CMOS image sensors with in-pixel temporal redundant samplings," *IEEE Trans. Electron Devices*, early access, Nov. 13, 2021, doi: 10.1109/TED.2021.3122394.

[3] V. Cornet, Y. Govaert, G. Moens, J. Van Loco, and J.-M. Degroodt, "Development of a fast analytical method for the determination of Sudan dyes in chili- and curry-containing foodstuffs by high-performance liquid chromatography–photodiode array detection," *J. Agricult. Food Chem.*, vol. 54, no. 3, pp. 639–644, Jan. 2006.

[4] R. Kuroda *et al.*, "A high quantum efficiency high readout speed 1024 pixel ultraviolet-visible-near infrared waveband photodiode array," *ITE Trans. Media Technol. Appl.*, vol. 4, no. 2, pp. 109–115, Apr. 2016.

[5] H. Ishii *et al.*, "A high-sensitivity compact gas concentration sensor using ultraviolet light absorption with a heating function for a high-precision trimethyl aluminum gas supply system," *Jpn. J. Appl. Phys.*, vol. 58, no. SB, Apr. 2019, Art. no. SBBL04.

[6] M. Mori *et al.*, "Thin organic photoconductive film image sensors with extremely high saturation of 8500 electrons/μm^2," in *Proc. Symp. VLSI Technol.*, Jun. 2021, pp. T22–T23.

[7] K. Nishimura *et al.*, "An 8K4K-resolution 60 fps 450 ke$^-$-saturation-signal organic-photoconductive-film global-shutter CMOS image sensor with in-pixel noise canceller," in *IEEE ISSCC Dig. Tech. Papers*, Feb. 2018, pp. 82–83.

[8] F. Lalanne, P. Malinge, D. Hérault, C. Jamin-Mornet, and N. Virollet, "A 750 K photocharge linear full well in a 3.2μm HDR pixel with complementary carrier collection," *Sensors*, vol. 18, no. 2, p. 305, Jan. 2018.

[9] S. Sugawa, N. Akahane, S. Adachi, K. Mori, T. Ishiuchi, and K. Mizobuchi, "A 100 dB dynamic range CMOS image sensor using a lateral overflow integration capacitor," in *IEEE ISSCC Dig. Tech. Papers*, Feb. 2005, p. 353.

[10] Y. Fujihara, M. Murata, S. Nakayama, R. Kuroda, and S. Sugawa, "An over 120 dB single exposure wide dynamic range CMOS image sensor with two-stage lateral overflow integration capacitor," *IEEE Trans. Electron Devices*, vol. 68, no. 1, pp. 152–157, Jan. 2021.

[11] M. Murata *et al.*, "A 24.3 Me$^-$ full well capacity CMOS image sensor with lateral overflow integration trench capacitor," *IEEE Trans. Electron Devices.*, vol. 67, no. 4, pp. 1653–1659, Apr. 2020.

[12] M. Suzuki *et al.*, "An over 1 Mfps global shutter CMOS image sensor with 480 frame storage using vertical analog memory integration," in *IEDM Tech. Dig.*, Dec. 2016, pp. 212–215.

[13] G. Park *et al.*, "A 2.2μm stacked back side illuminated voltage domain global shutter CMOS image sensor," in *IEDM Tech. Dig.*, Dec. 2019, pp. 378–381.

[14] J.-K. Lee *et al.*, "A 2.1e$^-$ temporal noise and -105 dB parasitic light sensitivity backside-illuminated 2.3μm-pixel voltage-domain global shutter CMOS image sensor using high-capacity DRAM capacitor technology," in *IEEE ISSCC Dig. Tech. Papers*, Feb. 2020, pp. 102–103.

[15] M. Takase *et al.*, "An over 120 dB wide-dynamic-range 3.0μm pixel image sensor with in-pixel capacitor of 41.7 fF/um^2 and high reliability enabled by BEOL 3D capacitor process," in *Proc. IEEE Symp. VLSI Technol.*, Jun. 2018, pp. 71–72.

[16] T. Oikawa *et al.*, "A 1000 fps high SNR voltage-domain global shutter CMOS image sensor with two-stage LOFIC for *in-situ* fluid concentration distribution measurements," in *Proc. IISW*, 2021, pp. 258–261.

[17] R. Kuroda *et al.*, "A highly ultraviolet light sensitive and highly robust image sensor technology based on flattened Si surface," *ITE Trans. Media Technol. Appl.*, vol. 2, no. 2, pp. 123–130, 2014.

[18] S. Nasuno, S. Wakashima, F. Kusuhara, R. Kuroda, and S. Sugawa, "A CMOS image sensor with 240μV/e-conversion gain, 200 ke$^-$ full well capacity and 190–1000 nm spectral response and high robustness to UV," *ITE Trans. Media Technol. Appl.*, vol. 4, no. 2, pp. 116–122, Apr. 2016.

[19] H. Shike *et al.*, "A global shutter wide dynamic range soft X-ray CMOS image sensor with backside- illuminated pinned photodiode, two-stage lateral overflow integration capacitor, and voltage domain memory bank," *IEEE Trans. Electron Devices*, vol. 68, no. 4, pp. 2056–2063, Apr. 2021.

[20] C. Liu *et al.*, "A 4.6μm, 512$\times$512, ultra-low power stacked digital pixel sensor with triple quantization and 127 dB dynamic range," in *IEDM Tech. Dig.*, Dec. 2020, pp. 327–330.

[21] K. Miyauchi *et al.*, "4.0μm stacked voltage mode global shutter pixels with a BSI LOFIC and a PDAF capability," in *Proc. IISW*, 2021, pp. 316–319.

[22] Y. Kumagai *et al.*, "Back-illuminated 2.74μm-pixel pitch global shutter CMOS image sensor with charge-domain memory achieving 10 ke$^-$ saturation signal," in *IEDM Tech. Dig.*, 2018, pp. 237–240.

[23] G. Meynants *et al.*, "A 47 Mpixel 36.4 $\times$ 27.6 mm^2 30 fps global shutter image sensor," in *Proc. IISW*, 2017, pp. 378–381.

[24] N. Akahane, K. Mizobuchi, S. Sugawa, and S. Adachi, "Optimum design of conversion gain and full well capacity in CMOS image sensor with lateral overflow integration capacitor," *IEEE Trans. Electron Devices*, vol. 56, no. 11, pp. 2429–2435, Nov. 2009.

[25] M. Oh *et al.*, "3.0μm backside illuminated, lateral overflow, high dynamic range, LED flicker mitigation on image sensor," in *Proc. IISW*, 2019, pp. 262–265.

[26] M. Innocent *et al.*, "Pixel with nested photo diodes and 120 dB single exposure dynamic range," in *Proc. IISW*, 2019, pp. 95–98.

[27] X. Wang, B. Wolfs, G. Meynants, and J. Bogaerts, "An 89 db dynamic range CMOS image sensor with dual transfer gate pixel," in *Proc. IISW*, 2011, pp. 248–251.

[28] J. Solhusvik *et al.*, "A 1392 $\times$ 976 2.8μm 120 dB CIS with per-pixel controlled conversion gain," in *Proc. IISW*, 2017, pp. 298–301.

[29] S. Iida *et al.*, "A 0.68 e-rms random-noise 121 dB dynamic-range sub-pixel architecture CMOS image sensor with LED flicker mitigation," in *IEDM Tech. Dig.*, Dec. 2018, pp. 221–224.